

Theoretical modelling of hydrodynamic characteristics of a combined column-plate structure based on a novel derivation of mean drift force formulation

Cong, Peiwen

State Key Laboratory of Coastal and Offshore Engineering, Dalian University of Technology

Liu, Yingyi

State Key Laboratory of Coastal and Offshore Engineering, Dalian University of Technology

Gou, Ying

Research Institute for Applied Mechanics, Kyushu University

Teng, Bin

State Key Laboratory of Coastal and Offshore Engineering, Dalian University of Technology

<https://hdl.handle.net/2324/3077408>

出版情報 : Proceedings of the Institution of Mechanical Engineers, Part M: Journal of Engineering for the Maritime Environment. 233 (4), pp.1022-1036, 2018-10-29. SAGE Publications
バージョン :
権利関係 : © 2018 by the author(s).

1 Theoretical modelling of hydrodynamic characteristics of a
2 combined column-plate structure based on a novel derivation of
3 mean drift force formulation

4
5 Peiwen Cong^{a*}, Yingyi Liu^{a, b}, Ying Gou^a and Bin Teng^a

6
7 ^a State Key Laboratory of Coastal and Offshore Engineering, Dalian University of Technology,
8 Dalian 116024, China

9 ^b Research Institute for Applied Mechanics, Kyushu University, Kasuga, Fukuoka 816-8580, Japan

10
11 **Abstract**

12 To improve the seakeeping capability, some devices, such as submerged plates, are
13 often installed on floating structures. The attached plate cannot only suppress the
14 motion response, but also provide an additional immersed body surface that receives
15 fluid action, aggravating the wave loads. In this study, a theoretical model is developed
16 within the context of linear potential theory to study the hydrodynamic characteristics
17 of a floating column with a submerged plate attached at the bottom. The eigenfunction
18 expansion matching method is applied to obtain the velocity potential, based on which
19 the linear wave force and wave runup can be found immediately. A novel derivation of
20 the mean drift force formulation is developed via the application of Green's second
21 identity to the velocity potential and its derivative in finite fluid volume surrounding
22 the body. Formulations that involve control surface can then be derived. With the
23 availability of the velocity potential, semi-analytical solution of the mean drift force on
24 the combined column-plate structure is developed based on respectively the derived
25 and the classic far-field formulations. After conducting convergence tests and validating
26 the theoretical model, detailed numerical analysis is performed thereafter based on the
27 theoretical model. The influence of the plate size, such as the radius and height, on the
28 wave force and the associated wave runup are assessed.

29 **Keywords:** Mean drift force; Submerged plate; Control surface; Wave runup

30

31 **1. Introduction**

32 A submerged plate can be frequently employed as an essential component of many
33 offshore structures, such as spar-type platform and floating wind turbines (FWTs)
34 ([Downie et al., 2000](#); [Li et al., 2013](#); [Antonutti et al., 2014](#)). Most proposed semi-
35 submersible FWTs are composed of columns and submerged plates installed at the
36 bottom providing support. The attached plates are designed to increase the added mass
37 and provide extra damping, without obviously changing the displacement or the column
38 size. Consequently, the natural frequency of the structure can be moved out of the
39 dominant frequency range of incident waves. Meanwhile, utilization of submerged
40 plates for other purposes including wave control and coastal morphology control are
41 also promising.

42 The problem of wave interaction with submerged plates has received considerable
43 attention from researchers. [Yu and Chwang \(1993\)](#) solved the wave scattering over a
44 submerged thin plate by means of eigenfunction expansion method. [Martin and Farina](#)
45 [\(1997\)](#) used the hypersingular integral equation to formulate the wave diffraction by a
46 thin plate close enough to the free surface. [Molin \(2001\)](#) proposed a theoretical model
47 to derive the added mass and damping coefficients of periodic arrays of plates. [Tao and](#)
48 [Thiagarajan \(2003a, 2003b\)](#) investigated the flow characteristics around an oscillating
49 plate by using the finite difference method. [Farina \(2010\)](#) examined the wave radiation
50 from an oscillating plate and derived an asymptotic approximation for cases of small
51 submergences. [Jiang et al. \(2014a, 2014b\)](#) established analytical solutions for the wave
52 diffraction and radiation problem by a submerged vertical cylinder. [Koh and Cho \(2016\)](#)
53 assessed the performance of double thin plates as motion reduction devices for spar-
54 type platforms. [Wang and Zhang \(2018\)](#) studied on the wave radiation problem by
55 double submerged inclined plates by use of the boundary element method.

56 Attaching a submerged plate to a floating body can increase the added mass and
57 provide additional damping. Meanwhile, it can also extend the wetted surface that

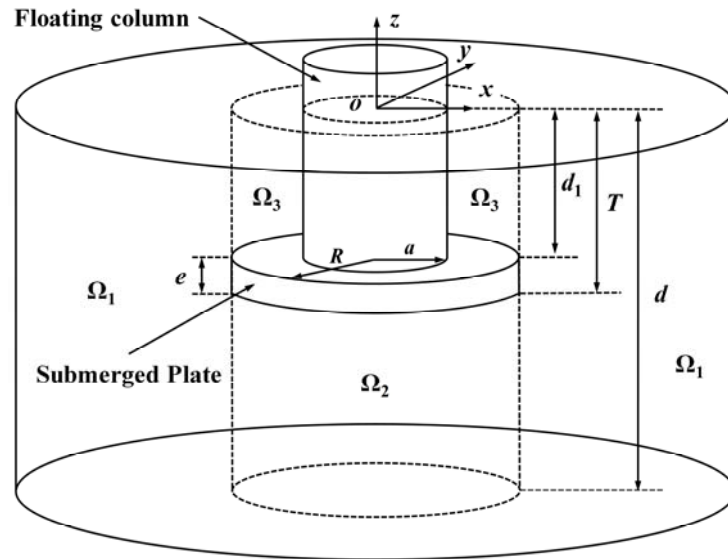
58 receives fluid loads, giving raise to additional excitations. Different from previous
59 studies, the main attention in this study has no longer been paid on the added mass and
60 damping coefficients associated with an attached plate and their effects on the motion
61 behavior. Instead, our aim is to study particularly the influence of the plate size, such
62 as the radius and height, on the wave force exert on the body and the associated wave
63 runup, which are also closely relevant to the structural design.

64 In this study, a theoretical model is developed within the context of linear potential
65 theory to study the wave interaction with a stationary combined column-plate structure.
66 The velocity potential is obtained by applying the eigenfunction expansion matching
67 method and the linear wave force and wave runup can be found immediately. The mean
68 drift force is due to the quadratic pressure distributed on the body surface. As remarked
69 in [Lee \(2007\)](#), singularities of the quadratic pressure are present near the hull area with
70 sharp variation of geometry, which makes it difficult to obtain accurate computational
71 results. This study intends to constitute a contribution for overcoming this difficulty.
72 The Green's second identity is applied to the velocity potential and its derivative in
73 finite fluid volume surrounding the body. Formulation that involves control surface can
74 then be derived and the integral on the body surface can be transferred to that written
75 on surfaces surrounding the body. Furthermore, the derived formulation is found to be
76 essentially identical with that in [Chen \(2006\)](#), which is developed by using the variants
77 of Stokes's and Gauss's theorem, for cases of stationary and wall-sided bodies. Semi-
78 analytical solutions of the mean drift force on the combined column-plate structure are
79 then developed based on respectively the derived and the classic far-field formulations.
80 After conducting convergence tests and validating the theoretical model, calculations
81 are conducted for various cases. It can be found that the existence of the plate can lead
82 to obvious amplification of the free-surface oscillation near the front and rear edges of
83 the column at specific frequencies. It is also shown that the in the vertical direction the
84 linear wave force and mean drift force can vanish in certain cases, which suggests that
85 the attached plate can be optimized to decrease the vertical force through adjusting the
86 design parameters.

87 The remaining part of the present paper is organized as follows: The mathematical

88 problem description is introduced in Section 2. The solution of the wave diffraction
 89 problem is presented in Section 3. The calculation of the linear wave force and wave
 90 runup is introduced in Section 4. The new derivation of the wave drift force formulation
 91 and the calculation of the mean drift force on the combined column-plate structure is
 92 introduced in detail in Section 5. Convergence test and validation of the theoretical
 93 model is given in Section 6. Numerical computation and analysis are carried out
 94 thereafter, with respect to a variety of geometrical parameters in Section 7. Conclusions
 95 have been drawn in Section 8 based on the previous analysis.

96



97

Fig. 1 Definition of the coordinate systems

98

99

100 2. Mathematical Problem

101 The wave diffraction by a circular column with a submerged plate is considered. The
 102 Oxy and $Or\theta$ planes are both located on the undisturbed free surface and the z -axis
 103 points vertically upward. A circular column with radius a and draft d_1 is floating in
 104 the fluid and its axis coincides with the z -axis. A submerged plate with radius R and
 105 height e , which is coaxial with the column, is attached at the bottom of the column
 106 rigidly. The clearance between the plate and seabed is $S = d - T$, where T is the draft of
 107 the whole structure and d is the constant water depth.

108 It is assumed that the fluid is inviscid and incompressible with a constant density ρ ,

109 the fluid motion is irrotational, and the wave steepness is small. Thus, the fluid velocity
 110 at time t is defined by the gradient of the velocity potential $\Phi(\mathbf{x}, t)$ satisfying Laplace's
 111 equation

$$112 \quad \nabla^2 \Phi(\mathbf{x}, t) = 0. \quad (1)$$

113 The velocity potential must satisfy appropriate boundary conditions, namely

$$114 \quad \frac{\partial^2 \Phi}{\partial t^2} + g \frac{\partial \Phi}{\partial z} = 0, \quad \text{on } z=0; \quad (2)$$

$$115 \quad \frac{\partial \Phi}{\partial z} = 0, \quad \text{on } z=-d; \quad (3)$$

$$116 \quad \frac{\partial \Phi}{\partial n} = 0, \quad \text{on } S_b, \quad (4)$$

117 Further, if the incident wave is time harmonic, the time factor can be separated out and
 118 the velocity potential is then expressed as

$$119 \quad \Phi(\mathbf{x}, t) = \text{Re}[\phi(r, \theta, z)e^{-i\omega t}], \quad (5)$$

120 where ω represents the wave angular frequency; $i = \sqrt{-1}$.

121 The presence of the fixed body in the fluid results in diffraction of the incident waves.
 122 Then the spatial velocity potential ϕ can be decomposed into the incident potential
 123 ϕ_I and the diffraction potential ϕ_D , i.e.,

$$124 \quad \phi(r, \theta, z) = \phi_I(r, \theta, z) + \phi_D(r, \theta, z). \quad (6)$$

125 Besides Eqs. (2), (3) and (4), ϕ_D has to satisfy the Sommerfeld radiation condition at
 126 a large radial distance from the structure.

127 Considering linear incident waves propagate to the positive x -direction, ϕ_I is given
 128 by:

$$129 \quad \phi_I(r, \theta, z) = \sum_{m=0}^{\infty} \varphi_{I,m}(r, z) \cos m\theta; \quad (7)$$

130 in which

$$131 \quad \varphi_{I,m}(r, z) = -\frac{iAg \cosh \kappa_0(z+d)}{\omega \cosh \kappa_0 d} \varepsilon_m i^m J_m(\kappa_0 r). \quad (8)$$

132 In Eq. (8), $\varepsilon_0 = 1$ and $\varepsilon_m = 2$ when $m \geq 1$; $J_m(x)$ are the Bessel functions of order
 133 m ; A is the amplitude of incident waves; g is the gravitational acceleration; κ_0 is the
 134 wave number, satisfying the dispersion relation $\omega^2 = g\kappa_0 \tanh \kappa_0 d$.

135

136 3. Solution of Wave Diffraction Problem

137 The whole fluid domain is divided into three subdomains, i.e., Ω_1 , Ω_2 and Ω_3 ,
 138 as shown in Fig. 1. Ω_1 is the exterior domain ($r \geq R, -d \leq z \leq 0$), Ω_2 is the domain
 139 below the plate ($0 \leq r \leq R, -d \leq z \leq -T$), and Ω_3 is the domain above the plate ($a \leq r$
 140 $\leq R, -d_1 \leq z \leq 0$). Hereinafter, ϕ_n ($n = 1, 2, 3$) is used to denote the spatial potential
 141 in these subdomains. By means of the eigenfunction expansion method (Yeung, 1981;
 142 Calisal and Sabuncu, 1984), ϕ_n can be expanded into Fourier-cosine series in terms of
 143 the circumferential coordinate θ

$$144 \quad \phi_n(r, \theta, z) = \sum_{m=0}^{\infty} \varphi_{n,m}(r, z) \cos m\theta, \quad n = 1, 2, 3, \quad (9)$$

145 where

$$146 \quad \varphi_{1,m}(r, z) = -\frac{iAg}{\omega} \varepsilon_m i^m \left[J_m(\kappa_0 r) Z_0(\kappa_0 z) + \sum_{j=0}^{\infty} A_{m,j} R_{m,j}(\kappa_j r) Z_j(\kappa_j z) \right]; \quad (10a)$$

$$147 \quad \varphi_{2,m}(r, z) = -\frac{iAg}{\omega} \varepsilon_m i^m \sum_{l=0}^{\infty} B_{m,l} V_{m,l}(\lambda_l r) Y_l(\lambda_l z); \quad (10b)$$

$$148 \quad \varphi_{3,m}(r, z) = -\frac{iAg}{\omega} \varepsilon_m i^m \sum_{k=0}^{\infty} C_{m,k} [\beta_{m,k} P_{m,k}(\mu_k r) + Q_{m,k}(\mu_k r)] U_k(\mu_k z). \quad (10c)$$

149 In Eq. (10), $A_{m,j}$, $B_{m,l}$ and $C_{m,k}$ are unknown coefficients; κ_j ($j \geq 1$) are positive
 150 real roots of $-\omega^2 = g\kappa_j \tan(\kappa_j d)$; the eigenvalues λ_l are defined as $\lambda_0 = 1$ and
 151 $\lambda_l = l\pi/S$ for $l \geq 1$; μ_0 and wave frequency ω satisfy the dispersion relation
 152 $\omega^2 = g\mu_0 \tanh(\mu_0 d_1)$; μ_k ($k \geq 1$) are positive real roots of $-\omega^2 = g\mu_k \tan(\mu_k d_1)$;
 153 $R_{m,j}(\kappa_j r)$, $V_{m,l}(\lambda_l r)$ and $P_{m,k}(\mu_k r)$ are radial functions, defined by

$$154 \quad R_{m,j}(\kappa_j r) = \begin{cases} H_m(\kappa_0 r), & j = 0, \\ K_m(\kappa_j r), & j \geq 1; \end{cases} \quad (11a)$$

$$155 \quad V_{m,l}(\lambda_l r) = \begin{cases} \left(\frac{r}{R}\right)^m, & l = 0, \\ \frac{I_m(\lambda_l r)}{I_m(\lambda_l R)}, & l \geq 1; \end{cases} \quad (11b)$$

$$156 \quad P_{m,k}(\mu_k r) = \begin{cases} J_m(\mu_0 r), & k = 0, \\ I_m(\mu_k r), & k \geq 1, \end{cases} \quad (11c)$$

157 in which, $H_m(x)$ are the first kind of Hankel functions of order m ; $I_m(x)$ and
 158 $K_m(x)$ are the first and second kinds of modified Hankel functions of order m ,
 159 respectively; $Q_{m,k}(\mu_k r)$ can be determined according to Eq. (11a) with κ_j and j
 160 replaced by μ_k and k respectively; the coefficient $\beta_{m,k}$ is defined as

$$161 \quad \beta_{m,k} = \begin{cases} -\frac{H'_m(\mu_0 a)}{J'_m(\mu_0 a)}, & k = 0, \\ -\frac{K'_m(\mu_k a)}{I'_m(\mu_k a)}, & k \geq 1, \end{cases} \quad (12)$$

162 where the prime appearing in the superscript denotes differentiation with respect to the
 163 argument; $Z_j(\kappa_j z)$, $Y_l(\lambda_l z)$ and $U_k(\mu_k z)$ are orthonormal functions given at the
 164 intervals $[-d, 0]$, $[-d, -T]$ and $[-d_1, 0]$ respectively, defined by

$$165 \quad Z_j(\kappa_j z) = \begin{cases} \frac{\cosh \kappa_0(z+d)}{\cosh \kappa_0 d}, & j = 0, \\ \frac{\cos \kappa_j(z+d)}{\cos \kappa_j d}, & j \geq 1; \end{cases} \quad (13a)$$

$$166 \quad Y_l(\lambda_l z) = \begin{cases} \frac{\sqrt{2}}{2}, & l = 0, \\ \cos \lambda_l(z+d), & l \geq 1; \end{cases} \quad (13b)$$

$$167 \quad U_k(\mu_k z) = \begin{cases} \frac{\cosh \mu_0(z+d_1)}{\cosh \mu_0 d_1}, & k = 0, \\ \frac{\cos \mu_k(z+d_1)}{\cos \mu_k d_1}, & k \geq 1. \end{cases} \quad (13c)$$

168 The expressions of the velocity potential are developed to satisfy Laplace's equation,

169 subjecting to all boundary conditions except that at the border of the subdomains, i.e.
 170 at $r = R$. The unknown coefficients in these expressions can be determined by imposing
 171 the matching condition at $r = R$, based on the assumption that the fluid pressure and the
 172 normal velocity are continuous across the border of neighboring subdomains. After
 173 truncating the infinite series of the orthogonal functions in Eq. (10) to finite terms, three
 174 sets of linear equations can be established containing an equivalent number of unknown
 175 coefficients. After solving the linear algebraic system, the unknown coefficients are
 176 found and the velocity potentials in each subdomain can be obtained.

177

178 **4. Calculation of the linear wave force and wave runup**

179 Once the velocity potential is obtained, some other physical quantities of interest may
 180 immediately be found. The linear wave runup along the cylinder, ζ , can be determined
 181 according to:

$$182 \quad \zeta = -\frac{1}{g} \frac{\partial \Phi}{\partial t}, \quad \text{on } z = 0. \quad (14)$$

183 The complex wave runup amplitude, η , is then given by:

$$184 \quad \eta = A \sum_{m=0}^{\infty} \varepsilon_m i^m \sum_{k=0}^{\infty} C_{m,k} [\beta_{m,k} P_{m,k}(\mu_k a) + Q_{m,k}(\mu_k a)] \cos m\theta. \quad (15)$$

185 The linear wave force is known by integrating the fluid pressure over the body
 186 surface. After integrating in θ and applying the orthogonal relationship, the horizontal
 187 force amplitude, f_x , can be expressed as

$$188 \quad f_x = -2iAg\rho\pi \left\{ R \left[J_1(\kappa_0 R) \hat{c}_0 + \sum_{j=0}^{\infty} A_{1,j} R_{1,j}(\kappa_j R) \hat{c}_j \right] \right. \\ \left. + a \sum_{k=0}^{\infty} C_{1,k} [\beta_{1,k} P_{1,k}(\mu_k a) + Q_{1,k}(\mu_k a)] \hat{d}_k \right\}, \quad (16)$$

189 in which

$$190 \quad \hat{c}_j = \begin{cases} \frac{\sinh \kappa_0 (d - d_1) - \sinh \kappa_0 S}{\kappa_0 \cosh \kappa_0 d}, & j = 0, \\ \frac{\sin \kappa_j (d - d_1) - \sin \kappa_j S}{\kappa_j \cos \kappa_j d}, & j \geq 1, \end{cases} \quad (17)$$

191 and

192
$$\hat{d}_k = \begin{cases} \frac{\tanh \mu_0 d_1}{\mu_0}, & k = 0, \\ \frac{\tan \mu_k d_1}{\mu_k}, & k \geq 1. \end{cases} \quad (18)$$

193 Similarly, the vertical force amplitude, f_z , can be written as

194
$$f_z = 2\pi\rho Ag \left[B_{0,0} \frac{\sqrt{2}}{4} R^2 + \sum_{l=1}^{\infty} \frac{B_{0,l} (-1)^l I_1(\lambda_l R) R}{\lambda_l I_0(\lambda_l R)} - \sum_{k=0}^N C_{0,k} \Pi_k \right], \quad (19)$$

195 in which

196
$$\Pi_k = \begin{cases} \frac{[\beta_{0,0} J_1(\mu_0 R) + H_1(\mu_0 R)] R - [\beta_{0,0} J_1(\mu_0 a) + H_1(\mu_0 a)] a}{\mu_0 \cosh \mu_0 d_1}, & k = 0, \\ \frac{[\beta_{0,k} I_1(\mu_k R) - K_1(\mu_k R)] R - [\beta_{0,k} I_1(\mu_k a) - K_1(\mu_k a)] a}{\mu_k \cos \mu_k d_1}, & k \geq 1. \end{cases} \quad (20)$$

197

198 5. Calculation of the wave drift loads

199 Three different methods have been developed so far for the computation of the mean
 200 drift force. The first one consists of direct pressure integrations on the hull of the body,
 201 as described in [Pinkster \(1980\)](#) and [Ogilvie \(1983\)](#), which is called the near-field
 202 formulation. The second one was derived in [Maruo \(1960\)](#) and [Newman \(1967\)](#) by
 203 applying the momentum theorem, which is called the far-field formulation. The third
 204 one was developed by using the variants of Stokes's and Gauss's theorem and takes
 205 advantage of a control surface at some distance from the body, as proposed in [Chen](#)
 206 [\(2006\)](#).

207 Referring to the established near-field formulation, the wave drift force on a
 208 stationary and wall-sided body can be computed by

209
$$\overline{\mathbf{f}^-} = -\frac{\rho}{2} \iint_{S_b} \nabla \Phi \cdot \nabla \Phi \mathbf{n} ds + \frac{\rho g}{2} \oint_{\Gamma} \zeta^2 \mathbf{n} dl, \quad (21)$$

210 in which all involved quantities in the integrand are of the first order; an over bar
 211 indicates the average over a wave period; Γ stands for the intersection of the body
 212 surface S_b with the mean free surface ($z = 0$); \mathbf{n} is the normal vector on S_b and it is
 213 positive when pointing out of the fluid domain. For wall-sided bodies, the normal vector

214 along Γ is the same as that on S_b at the same location. The near-field formulation is
 215 straightforward and can give all components of the mean drift force. However, for
 216 bodies have sharp corners, the quadratic pressure near the corner is singular and it is
 217 not easy to obtain accurate computational results through direct pressure integral.

218

219 **5.1 Calculation based on a novel derivation of wave drift loads formulation**

220 This study intends to constitute a contribution for overcoming above difficulty. After
 221 applying Stokes's theorem to a vector function \mathbf{B} , the following identity can be obtained:

$$222 \quad \iint_{S_b} \mathbf{n} \cdot (\nabla \times \mathbf{B}) ds = \oint_{\Gamma} \mathbf{B} \cdot \mathbf{t} dl, \quad (22)$$

223 in which, the line integral is taken in the counterclockwise sense about Γ ; \mathbf{t} is the unit
 224 vector tangent to Γ and oriented in the same direction as the path of integration. If the
 225 vector function \mathbf{B} is supposed to be $\Phi(\nabla\Phi \times \mathbf{e}_j)$ and the body-surface boundary
 226 condition, Eq. (4), is adopted, Eq. (22) can be written as:

$$227 \quad \iint_{S_b} (\nabla\Phi \cdot \nabla\Phi) n_j ds = \iint_{S_b} \Phi \frac{\partial}{\partial n} \left(\frac{\partial\Phi}{\partial x_j} \right) ds - \oint_{\Gamma} \Phi (\nabla\Phi \times \mathbf{e}_j) \cdot \mathbf{t} dl. \quad (23)$$

228 in which, \mathbf{e}_j ($j = 1, 2, 3$) represents the unit vectors in the x, y or z direction respectively;
 229 $x_1 = x, x_2 = y$, and $x_3 = z$; $n_1 = n_x, n_2 = n_y$, and $n_3 = n_z$.

230 A finite fluid volume limited by S_b, S_c , and S'_f is considered, in which S_c represents
 231 a fictitious (control) surface surrounding the body and S'_f is the mean free surface
 232 limited by Γ and the intersection of S_c with $z = 0$. As the velocity potential and its
 233 derivative both satisfy the Laplace's equation, by applying Green's second identify in
 234 the control fluid volume and making use of Eqs. (3) and (4), we can have:

$$235 \quad \iint_{S_b} \Phi \frac{\partial}{\partial n} \left(\frac{\partial\Phi}{\partial x_j} \right) ds = \iint_{S_c+S'_f} \left[\frac{\partial\Phi}{\partial x_j} \frac{\partial\Phi}{\partial n} - \Phi \frac{\partial}{\partial n} \left(\frac{\partial\Phi}{\partial x_j} \right) \right] ds. \quad (24)$$

236 Then Eq. (23) can be rewritten as:

$$237 \quad \iint_{S_b} (\nabla\Phi \cdot \nabla\Phi) n_j ds = \iint_{S_c+S'_f} \left[\frac{\partial\Phi}{\partial x_j} \frac{\partial\Phi}{\partial n} - \Phi \frac{\partial}{\partial n} \left(\frac{\partial\Phi}{\partial x_j} \right) \right] ds - \oint_{\Gamma} \Phi (\nabla\Phi \times \mathbf{e}_j) \cdot \mathbf{t} dl. \quad (25)$$

238 The integrals on the right-hand side of Eq. (25) contain second-order derivative of

239 the first-order velocity potential. As it is difficult to achieve high accuracy of the
 240 second-order derivative, care must be taken in dealing with these trouble terms. Based
 241 on the assumption that the control surface intersects vertically with $z = 0$, the integral
 242 over S_c can be expressed as one only containing the first-order derivative plus a line
 243 integral by use of Stokes's theorem:

$$244 \quad \iint_{S_c} \left[\frac{\partial \Phi}{\partial x_j} \frac{\partial \Phi}{\partial n} - \Phi \frac{\partial}{\partial n} \left(\frac{\partial \Phi}{\partial x_j} \right) \right] ds = \iint_{S_c} \left[2 \frac{\partial \Phi}{\partial x_j} \frac{\partial \Phi}{\partial n} - (\nabla \Phi \cdot \nabla \Phi) n_j \right] ds - \oint_{\Gamma_c} \Phi (\nabla \Phi \times \mathbf{e}_j) \cdot \mathbf{t} dl, \quad (26)$$

246 in which, Γ_c represents the intersection of S_c with $z = 0$ and the line integral is taken in
 247 the clockwise sense about Γ_c .

248 From Eq. (5), it is noted the velocity potential can be expressed in time-spatial
 249 decomposed form. For the case of $j = 1$, the integral over S'_f on the right-hand side of
 250 Eq. (25) can then be expressed as follows after imposing Eq. (2)

$$251 \quad \iint_{S'_f} \left[\frac{\partial \Phi}{\partial x} \frac{\partial \Phi}{\partial z} - \Phi \frac{\partial}{\partial z} \left(\frac{\partial \Phi}{\partial x} \right) \right] ds = \frac{1}{g} \iint_{S'_f} \frac{\partial}{\partial t} \left(-\frac{\partial \Phi}{\partial x} \frac{\partial \Phi}{\partial t} + \Phi \frac{\partial^2 \Phi}{\partial x \partial t} \right) ds. \quad (27)$$

252 It is obvious that the integral on the right-hand side of Eq. (27) gives zero mean in one
 253 period, which indicates

$$254 \quad \overline{\iint_{S'_f} \left[\frac{\partial \Phi}{\partial x} \frac{\partial \Phi}{\partial z} - \Phi \frac{\partial}{\partial z} \left(\frac{\partial \Phi}{\partial x} \right) \right] ds} = 0. \quad (28)$$

255 Therefore, for the case of $j = 1$, the integral over S'_f gives no contribution to the mean
 256 drift force. Meanwhile, for the case of $j = 3$, the integral over S'_f is possible to be
 257 expressed as one only containing the first-order derivative plus a line integral by use of
 258 Green's theorem. By imposing Eq. (4), the order of the derivatives can be reduced as
 259 follows:

$$260 \quad \iint_{S'_f} \left(\frac{\partial \Phi}{\partial z} \frac{\partial \Phi}{\partial z} - \Phi \frac{\partial^2 \Phi}{\partial z^2} \right) ds = \iint_{S'_f} \left[2 \frac{\partial \Phi}{\partial z} \frac{\partial \Phi}{\partial z} - (\nabla \Phi \cdot \nabla \Phi) n_z \right] ds + \oint_{\Gamma_c} \Phi \frac{\partial \Phi}{\partial n} dl, \quad (29)$$

261 in which, the line integral is taken in the counterclockwise sense about Γ_c .

262 Then by introducing Eq. (25) with $j = 1$ into Eq. (21) and making use of Eqs. (26)

263 and (28), the following formulation for f_x^- can be obtained.

$$264 \quad f_x^- = -\frac{\rho}{2} \overline{\iint_{S_c} \left[2 \frac{\partial \Phi}{\partial x} \frac{\partial \Phi}{\partial n} - (\nabla \Phi \cdot \nabla \Phi) n_x \right] ds} - \frac{\rho}{2} \oint_{\Gamma_c} \Phi \frac{\partial \Phi}{\partial z} n_x dl + \frac{\rho}{2} \oint_{\Gamma} \left(g \zeta^2 - \Phi \frac{\partial \Phi}{\partial z} \right) n_x dl. \quad (30)$$

265
266 If Eqs. (2) and (14) are adopted, the line integral along Γ in Eq. (30) can be further
267 expressed as:

$$268 \quad \oint_{\Gamma} \left(g \zeta^2 - \Phi \frac{\partial \Phi}{\partial z} \right) n_x dl = \frac{1}{g} \oint_{\Gamma} \frac{\partial}{\partial t} \left(\Phi \frac{\partial \Phi}{\partial t} \right) n_x dl. \quad (31)$$

269 It is obvious that the integral on the right-hand side in Eq. (31) gives zero mean in one
270 period, which indicates

$$271 \quad \overline{\oint_{\Gamma} \left(g \zeta^2 - \Phi \frac{\partial \Phi}{\partial z} \right) n_x dl} = 0. \quad (32)$$

272 Eq. (32) is also true with Γ replaced by Γ_c . Then by making use of Eq. (32), Eq. (30)
273 can be rewritten as

$$274 \quad f_x^- = -\frac{\rho}{2} \overline{\iint_{S_c} \left[2 \frac{\partial \Phi}{\partial x} \frac{\partial \Phi}{\partial n} - (\nabla \Phi \cdot \nabla \Phi) n_x \right] ds} - \frac{\rho g}{2} \oint_{\Gamma_c} \zeta^2 n_x dl. \quad (33)$$

275 By introducing Eq. (25) with $j=3$ into Eq. (21) and making use of Eqs. (26) and (29),
276 the following formulation for f_z^- can be obtained.

$$277 \quad f_z^- = -\frac{\rho}{2} \overline{\iint_{S_c + S'_f} \left[2 \frac{\partial \Phi}{\partial z} \frac{\partial \Phi}{\partial n} - (\nabla \Phi \cdot \nabla \Phi) n_z \right] ds}. \quad (34)$$

278 Thus, the mean drift force in the vertical direction is given by the integral on the control
279 surface S_c and the limited free surface S'_f .

280 Now the formulation for the computation of the wave drift force, Eqs. (33) and (34),
281 is derived based on the application of Green's second identity in a finite fluid volume
282 surrounding the body. It can be noted that the derived formulation is equivalent to that
283 obtained in Chen (2007) by using the variants of Stokes's and Gauss's theorem.

284

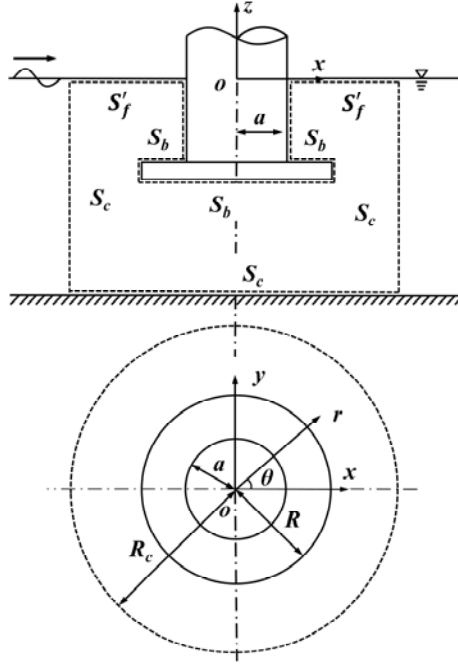


Fig. 2 Definition of control surface in the numerical implementation

285

286

287

288 With the availability of the velocity potential and based on the derived formulation,
 289 the mean drift force on the combined column-plate structure can be evaluated. The form
 290 of the control surface S_c can be arbitrary. To facilitate the numerical implementation,
 291 hereinafter, the control surface is made to be composed of a cylindrical surface defined
 292 by $r = R_c$ and $-d \leq z \leq 0$, and a limited sea-bed surface defined by $z = -d$ and $0 \leq r \leq R$.
 293 Fig. 2 gives the definition of the control surface in the numerical implantation. For
 294 vertically axisymmetric bodies, the surface integrals in Eqs. (33) and (34) can be
 295 reduced to line integrals after integrating in θ and applying orthogonality. Thus, by
 296 introducing Eqs. (9) and (10), the mean drift force on the combined column-plate
 297 structure can be calculated according to:

298

$$f_x^- = \text{Re} \left\{ -\frac{\rho\pi}{4} \sum_{m=0}^{\infty} \left[\int_{-d}^0 \hat{p}_{1,m}(R_c, z) dz + \hat{q}_{1,m}(R_c, 0) \right] \right\}; \quad (35)$$

299

$$f_z^- = \text{Re} \left\{ -\frac{\rho\pi}{4} \sum_{m=0}^{\infty} \left[\int_{-d}^0 \hat{u}_{1,m}(R_c, z) dz + \int_a^R \hat{v}_{3,m}(r, 0) dr + \int_R^{R_c} \hat{v}_{1,m}(r, 0) dr \right. \right. \\ \left. \left. + \int_0^R \hat{w}_{2,m}(r, -d) dr + \int_R^{R_c} \hat{w}_{1,m}(r, -d) dr \right] \right\}, \quad (36)$$

300 in which

$$301 \quad \hat{p}_{n,m}(r, z) = \frac{2}{\varepsilon_m} \left(\frac{\partial \varphi_{n,m}}{\partial r} \frac{\partial \varphi_{n,m+1}^*}{\partial r} + \frac{m+1}{r} \varphi_{n,m+1} \frac{\partial \varphi_{n,m}^*}{\partial r} - \frac{m}{r} \varphi_{n,m} \frac{\partial \varphi_{n,m+1}^*}{\partial r} \right. \\ \left. - \frac{m}{r} \frac{m+1}{r} \varphi_{n,m} \varphi_{n,m+1}^* - \frac{\partial \varphi_{n,m}}{\partial z} \frac{\partial \varphi_{n,m+1}^*}{\partial z} \right) r; \quad (37a)$$

$$302 \quad \hat{q}_{n,m}(r, z) = \frac{2}{\varepsilon_m} \left(\frac{\omega^2}{g} \varphi_{n,m} \varphi_{n,m+1}^* \right) r, \quad (37b)$$

303 and

$$304 \quad \hat{u}_{n,m}(r, z) = \frac{2}{\varepsilon_m} \left(2 \frac{\partial \varphi_{n,m}}{\partial z} \frac{\partial \varphi_{n,m}^*}{\partial r} \right) r; \quad (38a)$$

$$305 \quad \hat{v}_{n,m}(r, z) = \frac{2}{\varepsilon_m} \left(\frac{\omega^4}{g^2} \varphi_{n,m} \varphi_{n,m}^* - \frac{\partial \varphi_{n,m}}{\partial r} \frac{\partial \varphi_{n,m}^*}{\partial r} - \frac{m^2}{r^2} \varphi_{n,m} \varphi_{n,m}^* \right) r; \quad (38b)$$

$$306 \quad \hat{w}_{n,m}(r, z) = \frac{2}{\varepsilon_m} \left(\frac{\partial \varphi_{n,m}}{\partial r} \frac{\partial \varphi_{n,m}^*}{\partial r} + \frac{m^2}{r^2} \varphi_{n,m} \varphi_{n,m}^* \right) r. \quad (38c)$$

307 In Eqs. (35) and (36), ‘Re’ indicates that the real part is to be taken. In the numerical
308 implementation, Romberg quadrature method is used to control the accuracy of the line
309 integral in Eqs. (35) and (36).

310

311 5.2 Calculation based on the classic far-field formulation

312 The mean drift force can also be deduced from the quantities at far field. The far-
313 field formulation is restricted to give the components in the horizontal directions and
314 the moment around vertical axis. The expression of f_x^- given in Mei et al. (2005) is
315 reported below:

$$316 \quad f_x^- = - \overline{\iint_{S_\infty} [P \cos \theta + \rho U_r (U_r \cos \theta - U_\theta \sin \theta)] ds}, \quad (39)$$

317 in which, S_∞ is a cylindrical surface located at infinity; \mathbf{U} denotes the fluid velocity
318 and can be expressed in terms of gradient of the velocity potential; P is the pressure
319 term on the control surface and can be determined based on Bernoulli equation. With
320 all these manipulations, the following expression can be obtained (Mei, et al, 2005):

$$f_x^- = - \int_0^{2\pi} \rho r d\theta \cos \theta \left\{ \int_{-d}^0 dz \frac{1}{2} \left[\overline{\left(\frac{\partial \Phi}{\partial r} \right)^2} - \overline{\left(\frac{\partial \Phi}{\partial z} \right)^2} \right] + \frac{\omega^2}{4g} |\phi|_{z=0}^2 \right\}, \quad (40)$$

in which, r tends to infinity. At far field, the contribution from the evanescent modes to the diffraction potential is neglected. By using the asymptotic expressions for Bessel functions, the diffraction potential for large r can be expressed in an asymptotic form.

When the wave interaction with the combined column-plate structure is considered, ϕ_1 at far field is given by:

$$\phi_1 = - \frac{igA}{\omega} \left[e^{i\kappa_0 r \cos \theta} + \sqrt{\frac{2}{\pi \kappa_0 r}} e^{i\left(\kappa_0 r - \frac{\pi}{4}\right)} \sum_{m=-\infty}^{+\infty} \Lambda_m \cos m\theta \right] Z_0(\kappa_0 z), \quad (41)$$

in which,

$$\Lambda_m = \varepsilon_m i^m A_{m,0} e^{-\frac{m\pi}{2}i}. \quad (42)$$

By inserting Eq. (41) into Eq. (40) and applying the stationary phase method to the integrals, Eq. (40) can be rewritten as

$$f_x^- = - \frac{\rho g A^2}{\kappa_0} \frac{2\kappa_0 d + \sinh 2\kappa_0 d}{2 \sinh 2\kappa_0 d} \operatorname{Re} \left[\sum_{m=0}^{+\infty} 2 \left(\frac{1}{\varepsilon_m} \Lambda_m \Lambda_{m+1}^* + \Lambda_m \right) \right]. \quad (43)$$

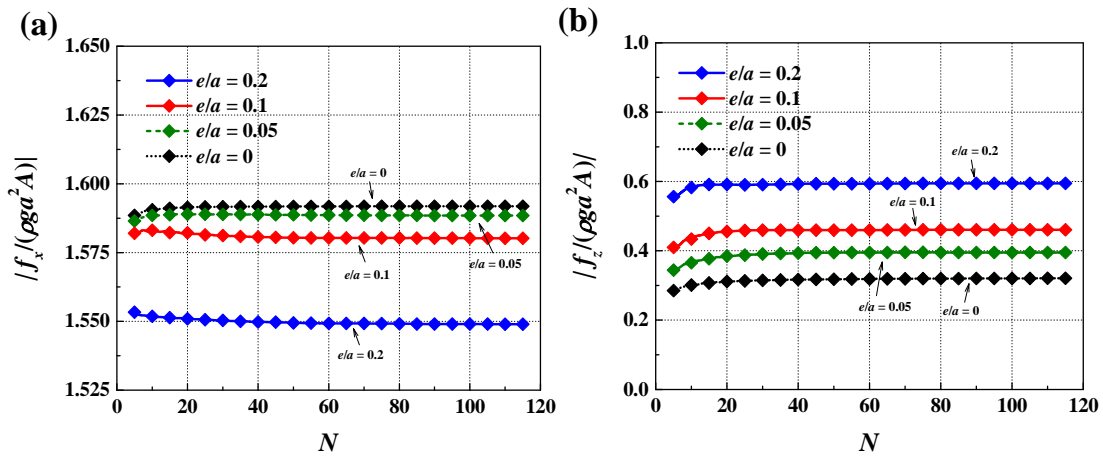
333

334 6. Convergence Test and Validation

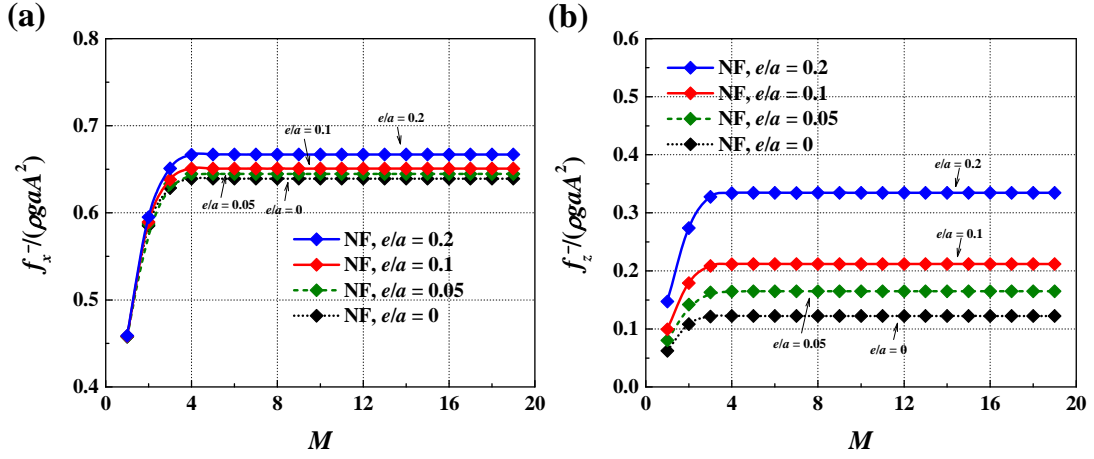
335 In order to ensure that present results are free from the influence of the truncation
 336 number, convergence of the theoretical model is examined. Hereinafter, $\rho g a^2 A$ and
 337 $\rho g a A^2$ are used to nondimensionalize the linear and mean drift force respectively. As
 338 illustrated in Bachynski et al. (2014), the dimensional supporting-column diameter in a
 339 wind turbine system can be around 12 m. The examination considers the cases that the
 340 draft of the structure keeps unchangeable at $T/a = 1$ and the plate radius keeps 1.5 times
 341 the column radius ($R/a = 1.5$). At the meantime, the plate height varies as $e/a = 0, 0.05,$
 342 0.1 and 0.2 . The water depth is constant as $d/a = 3$. The accuracy of the calculation for
 343 the linear wave force is mainly influenced by the number of eigenmodes N . Fig. 3 shows
 344 the linear wave force amplitude with varying N . As to the calculation of the mean drift
 345 force, not only the number of eigenmodes N , but also that of Fourier modes M , can

346 affect the accuracy. Figs. 4-6 present the examination on the convergence of the mean
 347 drift force with respect to varying M and N . In these figures, the mean drift force results
 348 based on the derived and the classic far-field formulations are referred as ‘NF’ and ‘FF’
 349 respectively. It can be seen that, regardless of the size of the structure, the convergence
 350 is satisfactory. Moreover, it can be concluded that 15 Fourier coefficients and 100
 351 eigenmodes are sufficient to guarantee a satisfactory accuracy. Therefore, $M = 15$ and
 352 $N = 100$ are used in all the subsequent computations.

353 The dependence of the calculation on the control surface is then examined when the
 354 derived mean drift force formulation is used. Fig. 7 presents the mean drift force results
 355 for different cases of control surface, in which R_c is varied as $R + d$, $R + 2d$ and $R + 5d$.
 356 $R_c = R + d$ has been used in the previous convergence test. It can be seen the different
 357 cases give almost the same results and $R_c = R + d$ is then used in all the subsequent
 358 computations. Furthermore, in order to make sure that the theoretical model is valid and
 359 reliable to a convinced degree, a comparison between the mean drift force results based
 360 on the derived and the classic far-field formulations is made. From the comparison
 361 listed in Table 1, it can be noted excellent agreement is obtained between the results.

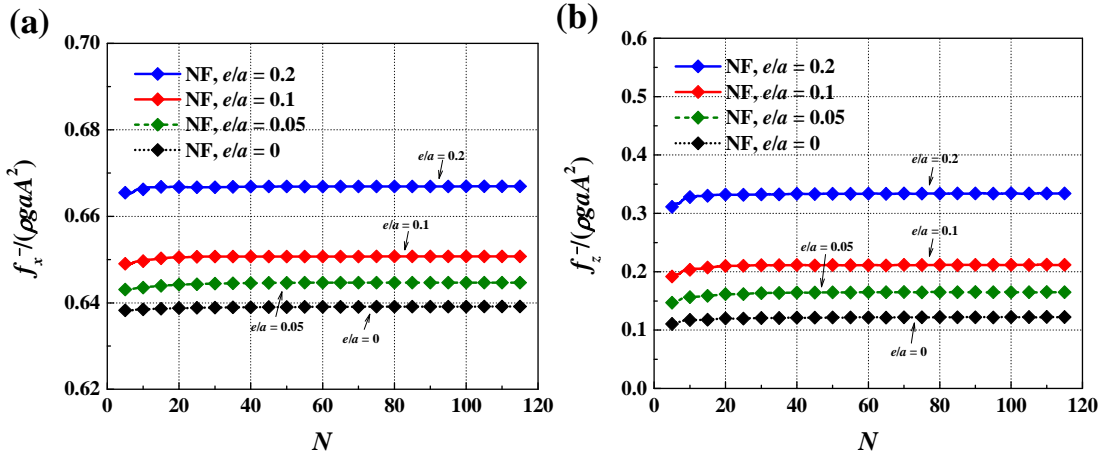


362
 363 Fig. 3 Convergence test on the linear wave force amplitude with respect to the number of
 364 eigenmodes N at $\kappa_0 a = 2.0$ ($T/a = 1$, $R/a = 1.5$, $d/a = 3$) (a) horizontal force (b) vertical force



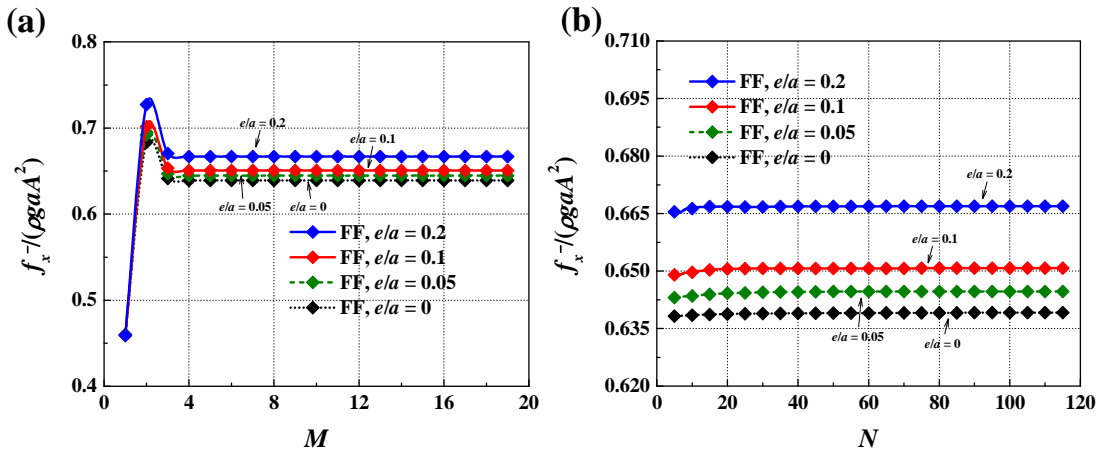
365

366 Fig. 4 Convergence test on the mean drift force based on the derived formulation with respect to
 367 the number of Fourier modes M at $\kappa_0 a = 2.0$ ($T/a = 1$, $R/a = 1.5$, $d/a = 3$) (a) horizontal force (b)
 368 vertical force



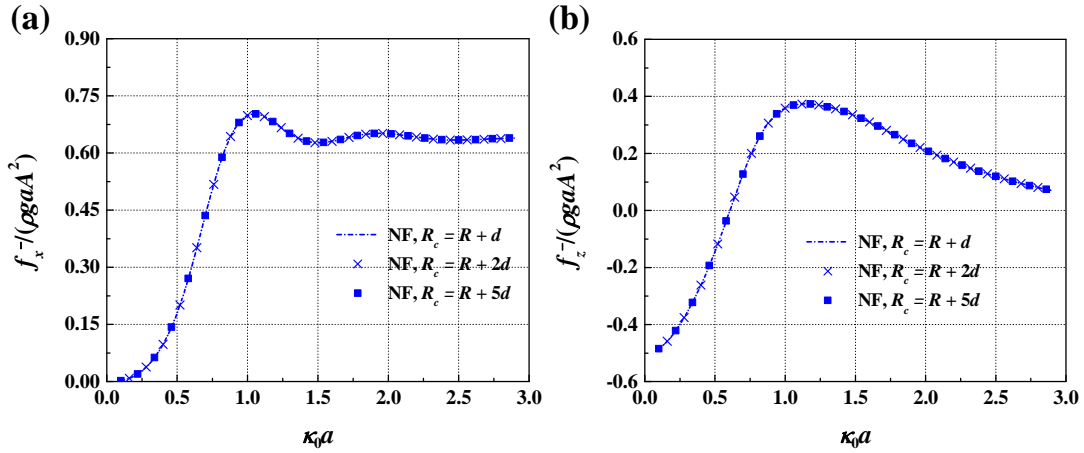
369

370 Fig. 5 Convergence test on the mean drift force based on the derived formulation with respect to
 371 the number of eigenmodes N at $\kappa_0 a = 2.0$ ($T/a = 1$, $R/a = 1.5$, $d/a = 3$) (a) horizontal force (b)
 372 vertical force



373

374 Fig. 6 Convergence test on the mean drift force based on the far-field formulation with respect to
 375 the number of Fourier modes M and eigenmodes N at $\kappa_0 a = 2.0$ ($T/a = 1$, $R/a = 1.5$, $d/a = 3$) (a) M
 376 (b) N



377
378 Fig. 7 Comparison of the mean drift force based on different values of R_c at $\kappa_0 a = 2.0$ ($T/a = 1$, R/a
379 $= 1.5$, $e/a = 0.1$, $d/a = 3$) (a) horizontal force (b) vertical force
380

381 Table 1 Comparison of the normalized mean drift force, $f_x^- / (\rho g a A^2)$, based on the derived and
382 the far-field formulations at different wave frequencies ($T/a = 1$, $R/a = 1.5$, $d/a = 3$)

$\kappa_0 a =$	$e/a = 0$		0.05		0.1		0.2	
	NF	FF	NF	FF	NF	FF	NF	FF
1.0	0.664	0.664	0.682	0.682	0.699	0.699	0.738	0.738
1.2	0.654	0.654	0.666	0.666	0.677	0.677	0.704	0.704
1.4	0.617	0.617	0.625	0.625	0.633	0.633	0.653	0.653
1.6	0.615	0.615	0.622	0.622	0.631	0.631	0.653	0.653
1.8	0.632	0.632	0.639	0.639	0.647	0.647	0.668	0.668
2.0	0.639	0.639	0.645	0.645	0.651	0.651	0.667	0.667

383

384 7. Numerical Results and Discussion

385 A comprehensive study is then performed to discuss the effects of the attached plate
386 on the wave force and the associated wave runoff. In all the subsequent calculations, the
387 draft of structure keeps constant as $T/a = 1$ and the water depth is $d/a = 3$.

388

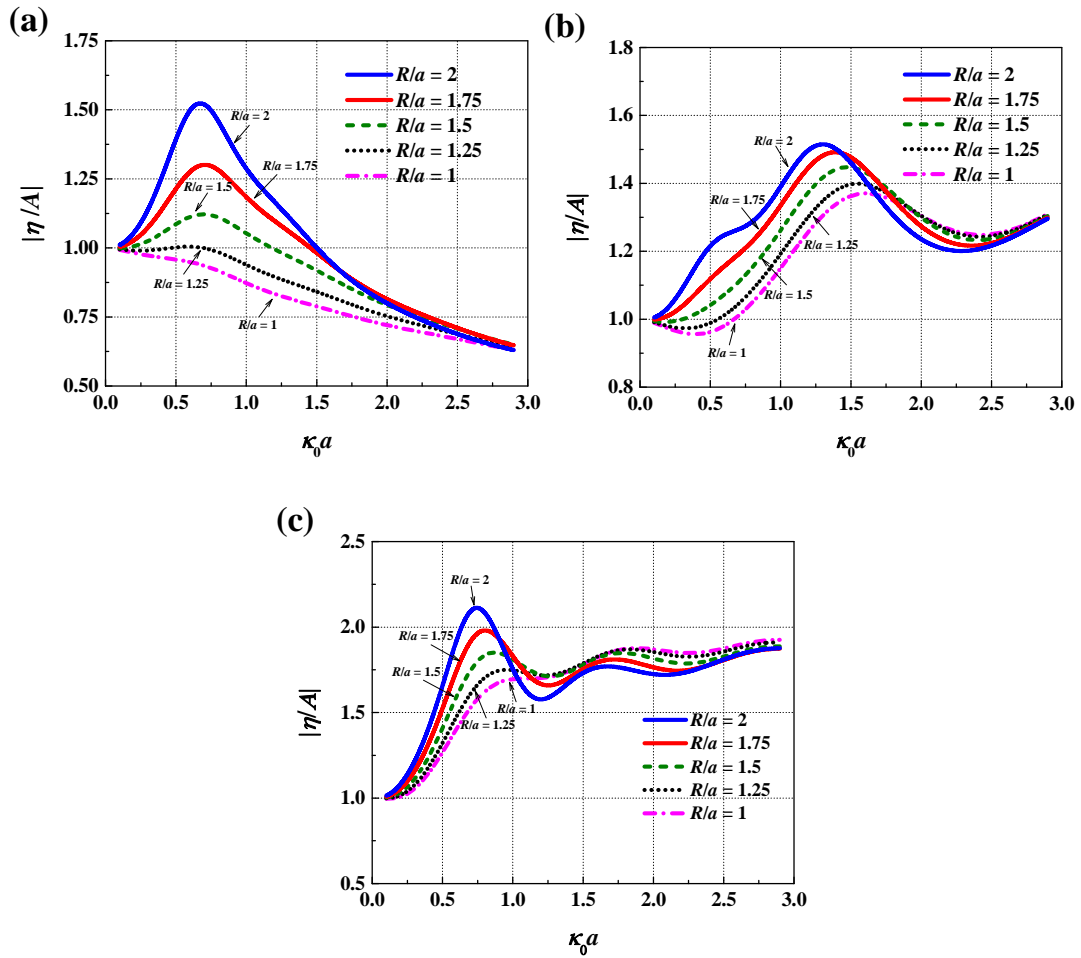
389 7.1 Linear Wave Runup

390 The effects of the attached plate on the linear wave runup amplitude at three different
391 locations around the body are shown in Fig. 8. The wave runup amplitude is plotted
392 versus the normalized wave number $\kappa_0 a$ in the cases of varying radius R and a constant
393 plate height $e/a = 0.1$. All curves in Fig. 8 are asymptotically getting close to 1 as $\kappa_0 a$
394 approaches zero, a state of no wave transformation at all.

395 A larger plate radius can cause a larger wave runup at the rear edge of the column (r

396 = a , $\theta = 0$, see Fig. 8(a)). From Fig. 8(a), it is also found that the wave runup amplitude
397 is always less than that of incident waves when $R = a$. However, this is not the case
398 when $R > a$. An obviously amplified wave runup occurs around $\kappa_0 a = 0.67$ when $R > a$,
399 and the amplification gradually weakens as R decreases. After shoaling into shallower
400 region over the plate, waves would undergo complicated transfer process. As pointed
401 by Yu (2002) in studying the wave scattering by a submerged plate that such transfer
402 process could induce obvious amplification of the free-surface oscillation over the plate
403 due to the phase interaction between the flows over and below the plate. Therefore,
404 obviously amplified wave runup can be observed in this study after including the effects
405 of the plate. Beyond the peak point, the wave runup amplitude decays quickly as $\kappa_0 a$
406 increases until less than that of incident waves. This can be attributed to the sheltering
407 effects provided by the column to the rear zone behind the structure. In Fig. 8(b), each
408 curve is characterized by an obvious peak, which gradually decreases and moves to the
409 high frequency region as R decreases. Beyond that peak point, influence from the plate
410 radius tends to be minor. At the front edge of the column ($r = a$, $\theta = \pi$, see Fig. 8(c)),
411 the wave runup firstly grows quickly until reaches the peak, which is reduced as the
412 radius of the plate approaches that of the column. Beyond the peak point, the wave
413 runup firstly falls quickly and then tends to behave stable in the high frequency region.

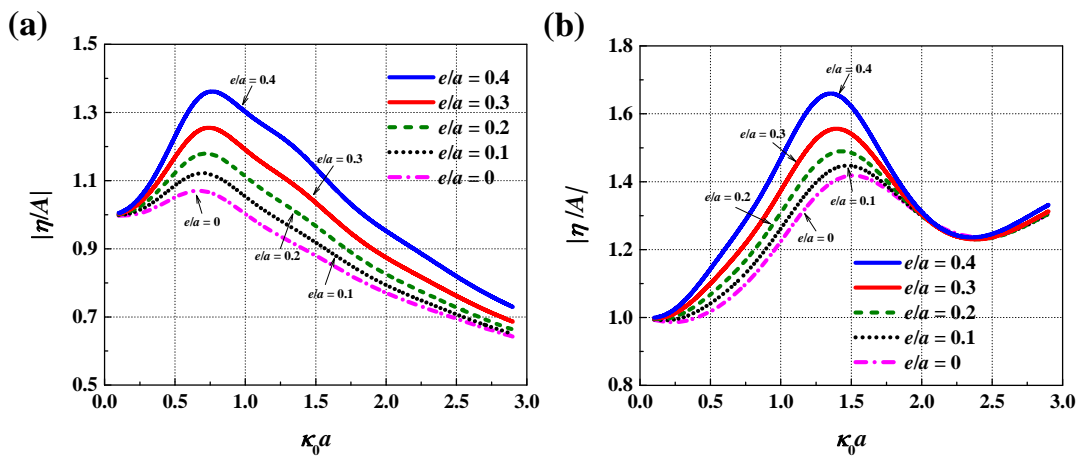
414 Fig. 9 presents the linear wave runup amplitude at three selected locations for
415 different plate height e with the plate radius keeps constant as $R/a = 1.5$. Effects of the
416 plate height are similar to that of the plate radius. Generally, when getting closer to the
417 free surface, the plate can have more significant effects on the wave scattering process
418 by the structure, which is a consequence of the exponential decay of wave motion in
419 the gravity direction.



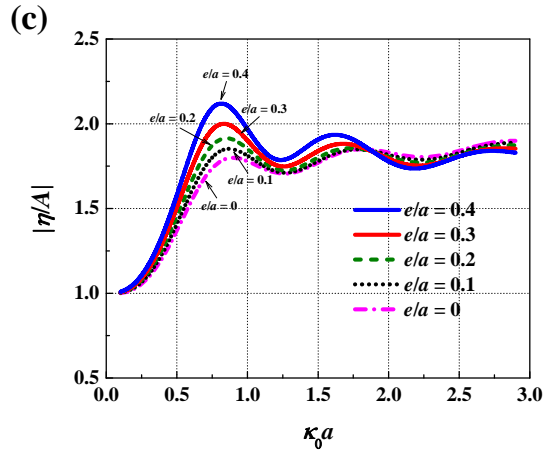
420

421

422 Fig. 8 Normalized linear wave runup amplitude at three locations around the body with different
 423 plate radius ($T/a = 1$, $e/a = 0.1$, $d/a = 3$) (a) $r = a$, $\theta = 0$ (b) $r = a$, $\theta = \pi/2$ (c) $r = a$, $\theta = \pi$



424



425

426 Fig. 9 Normalized linear wave runup amplitude at three locations around the body with different

427 plate height ($T/a = 1, R/a = 1.5, d/a = 3$) (a) $r = a, \theta = 0$ (b) $r = a, \theta = \pi/2$ (c) $r = a, \theta = \pi$

428

429 The distribution of the wave elevation amplitude around the body is plotted in Figs.

430 10-12 for $\kappa_0 a = 0.67, 0.74$ and 1.5 respectively with the plate height fixed at $e/a = 0.1$

431 and the plate radius varies as $R/a = 1, 1.5$ and 2 . All wave patterns are characterized by

432 obviously amplified free-surface oscillation near the front edge. At $\kappa_0 a = 0.67$ and 0.74

433 (see Figs. 11-12), the wave elevation around the front and the rear edges shows an

434 increasing tendency as R increases. In addition, at $\kappa_0 a = 0.67$ and 0.74 , the increase of

435 R leads to obvious changes in the wave pattern in the downstream region. Meanwhile,

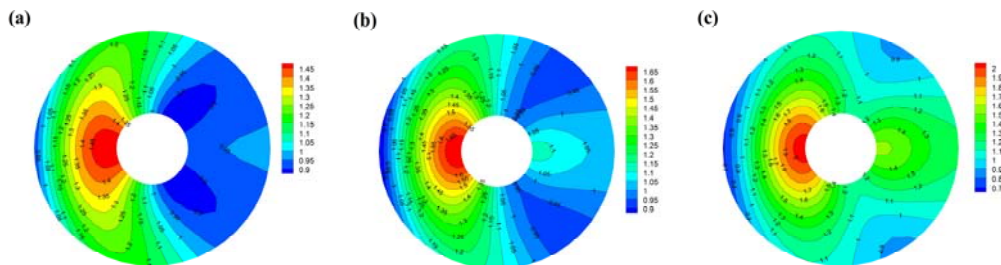
436 the wave elevation and its distribution at $\kappa_0 a = 1.5$ (see Fig. 13) appears to be less

437 dependent on the plate radius. This may be due to the fact that the wave motion

438 attenuates more rapidly in the gravity direction as the wave length decreases. Short

439 waves may not experience strong interaction with a plate submerged at a certain depth

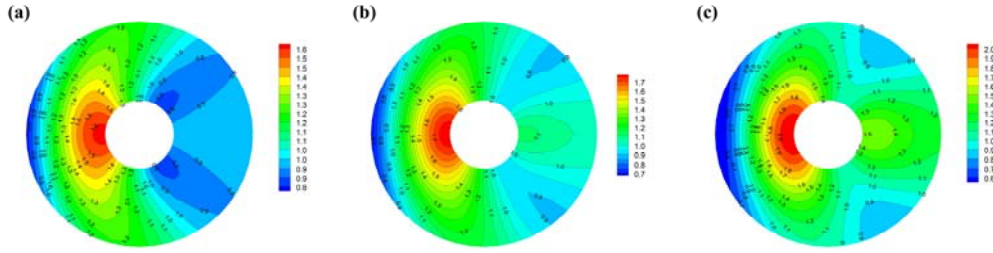
440 and then obvious disturb on the wave field cannot be induced.



441

442 Fig. 10 Distribution of the normalized wave elevation amplitude around the body at $\kappa_0 a = 0.67$

443 ($T/a = 1, e/a = 0.1, d/a = 3$) (a) $R/a = 1$ (b) $R/a = 1.5$ (c) $R/a = 2$

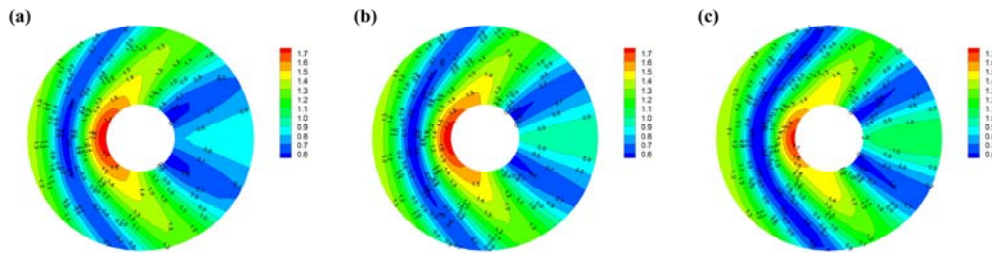


444

445 Fig. 11 Distribution of the normalized wave elevation amplitude around the body at $\kappa_0 a = 0.74$

446

($T/a = 1, e/a = 0.1, d/a = 3$) (a) $R/a = 1$ (b) $R/a = 1.5$ (c) $R/a = 2$



447

448 Fig. 12 Distribution of the normalized wave elevation amplitude around the body at $\kappa_0 a = 1.5$ (T/a

449

$= 1, e/a = 0.1, d/a = 3$) (a) $R/a = 1$ (b) $R/a = 1.5$ (c) $R/a = 2$

450

451 7.2 Linear Wave Force

452

453

454

455

456

457

458

459

460

461

462

463

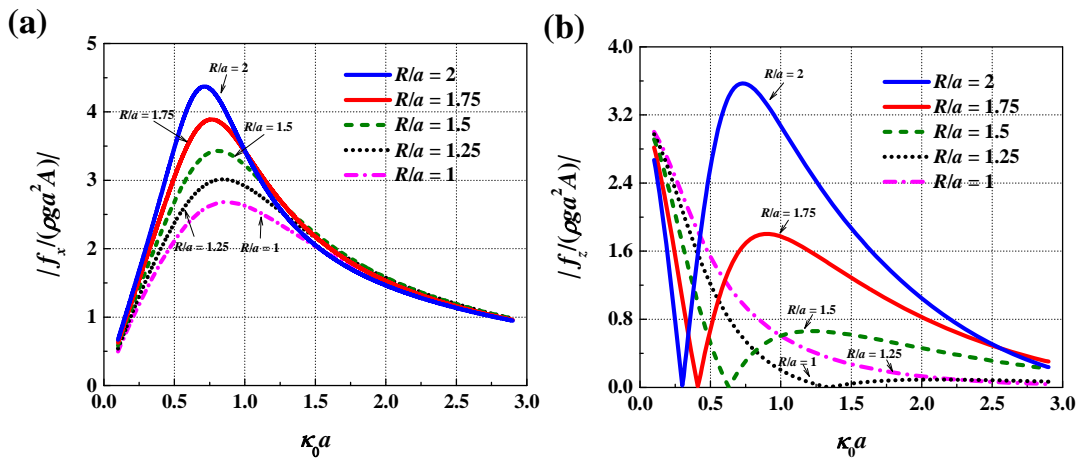
464

465

The variation of the linear wave force amplitude is shown in Fig. 13 for different plate radius R with the plate height being constant as $e/a = 0.1$. Note from Fig. 13(a) that regardless of the plate height the horizontal force firstly increases quickly until it reaches the maximum, and then decreases continuously as $\kappa_0 a$ increases further. The hydrodynamic pressure along the waterline is directly proportional to the wave elevation. When $R = a$, the peak value occurs around $\kappa_0 a = 0.87$, at which the relative phase between the wave elevation around the front and the rear edges is 158 degrees. It corresponds to the situation that that when a wave crest appears around the front edge, leading to positive hydrodynamic pressure, negative pressure occurs simultaneously around the rear edge. In addition, when the peak value occurs at $R = a$, an increase in R can amplify the free-surface oscillation around the front and rear edges and increase their relative phase gradually at the mean time, which can give rise to the increase of the horizontal wave force. Therefore, the peak values in Fig. 13(a) increase as R increases. Note from Fig. 13(b) that the vertical force decreases continuously as $\kappa_0 a$

466 increases when there is no plate attached to the column ($R = a$). Things become different
 467 when $R > a$, as there exist a zero-excitation frequency at which the structure endures no
 468 vertical excitation force. Basically, the vertical force can be divided into two parts, one
 469 the force on the bottom of the plate and the other the opposite one on the upper surface
 470 of the plate. The summation of the two parts can reach zero when they have the same
 471 magnitude. The zero-excitation frequency, moves gradually to the low frequency region
 472 as R increases. Before the zero-excitation point, an attached plate with larger radius
 473 endures smaller vertical force, while beyond that point such tendency is reversed but
 474 more pronounced.

475 Fig. 14 presents the linear wave force amplitude for different plate height e with the
 476 plate radius being constant as $R/a = 1.5$. In Fig. 14, the variation trend of the results
 477 with $\kappa_0 a$ is typical similar to that in Fig. 13. The horizontal force in general increases
 478 as e increases at a fixed wave frequency. Again, the vertical force is found to be zero at
 479 specific frequencies which gradually moves to the low frequency region as the plate
 480 height increases.



481

482 Fig. 13 Normalized linear wave force amplitude with different plate radius ($T/a = 1$, $e/a = 0.1$, d/a
 483 $= 3$) (a) horizontal force (b) vertical force

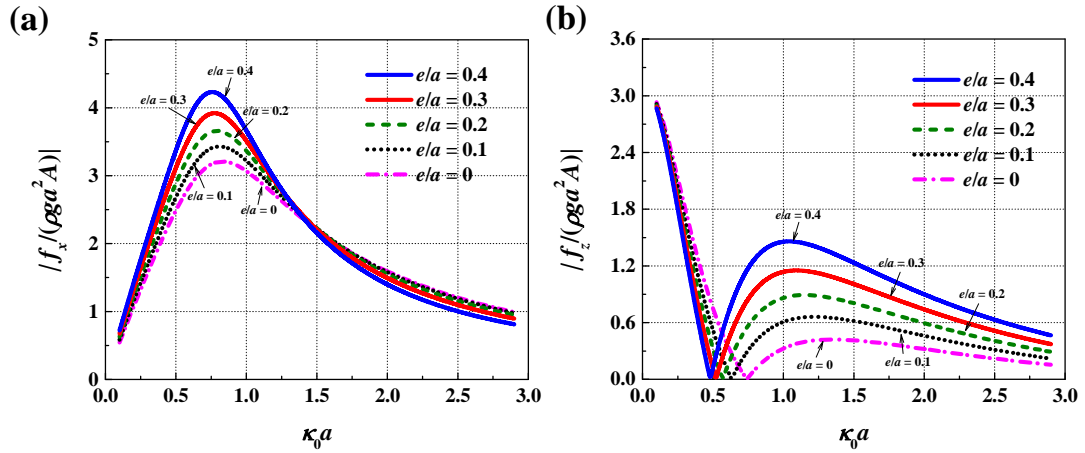


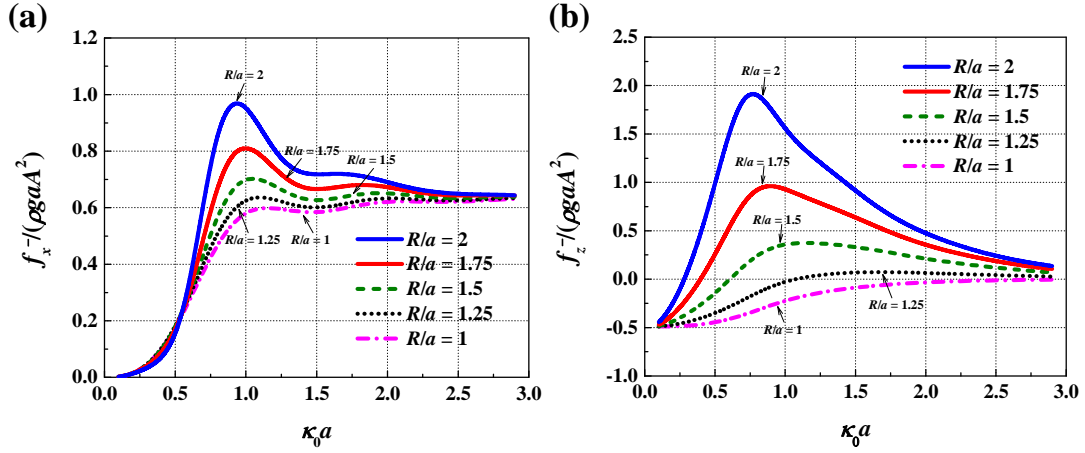
Fig. 14 Normalized linear wave force amplitude with different plate height ($T/a = 1$, $R/a = 1.5$, $d/a = 3$) (a) horizontal force (b) vertical force

7.3 Mean Drift Force

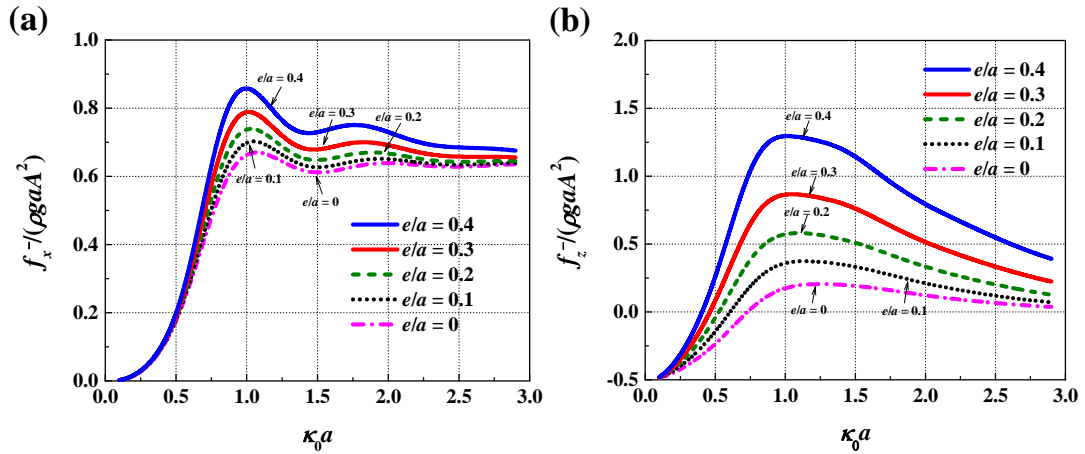
The influence of the plate radius on the mean drift force is examined in Fig. 15 with the plate height fixed at $e/a = 0.1$. The results given in this section are all obtained based on the derived mean drift force formulation. In Fig. 15(a), the mean drift force in the horizontal direction in general increases as R increases at a fixed wave frequency. As shown in Eq. (33), the mean drift force in the horizontal direction can be split into two terms: one written on the control surface and the other the wave elevation term. The two terms decrease to zero in the zero-frequency limit and then follow opposite variation trend with $\kappa_0 a$. In the high frequency region, their joint contribution is nearly constant, leading to the overall force tends to behave stable. From Fig. 15(b), it is noted that mean drift force in the vertical direction is in the negative z -direction over the entire frequency domain when $R = a$. This does not hold true when $R > a$. Apparently, the vertical mean drift force is contributed by two opposite parts which are associated with the wave action over the upper and bottom surfaces of the plate respectively. The overall force is firstly dominated by the later part which remains negative over all frequencies and its magnitude gradually decreases to zero as $\kappa_0 a$ increases. As $\kappa_0 a$ increases further, the former part becomes predominant, leading to the overall force in the positive z -direction. From Fig. 15(b), it is also noted that a larger plate radius results in more prominent variation against $\kappa_0 a$.

The variation of the mean drift force against the plate height e is shown in Fig. 16

508 when the plate radius keeps constant as $R/a = 1.5$. Effects of the plate height are similar
 509 to that of the plate radius. Generally, shallower heave plates (larger e) can more
 510 effectively interact with surface waves to affect the wave scattering process. Therefore,
 511 a plate with a larger height can impose more significant effects on the force.



512
 513 Fig. 15 Normalized mean drift force with different plate radius ($T/a = 1, e/a = 0.1, d/a = 3$) (a)
 514 horizontal force (b) vertical force



515
 516 Fig. 16 Normalized mean drift force with different plate height ($T/a = 1, R/a = 1.5, d/a = 3$) (a)
 517 horizontal force (b) vertical force

518

519 8. Conclusions

520 Wave interaction with a floating column with a submerged plate attached at the
 521 bottom is investigated through applying a theoretical model. Emphasis of this study has
 522 been laid on the influence of the attached plate on the wave force and the associated
 523 wave runup. Extensive calculations have been conducted with a variety of geometrical
 524 parameters. The main conclusions can then be summarized as follows:

525 1) A novel derivation of the mean drift force formulation is developed based on the

526 application of the Green's second identity to the velocity potential and its derivative in
527 finite fluid volume surrounding the body. The derived formulation involves control
528 surfaces at a distance from the body and is found to be essentially identical with that in
529 [Chen \(2006\)](#), which is developed by using the variants of Stokes's and Gauss's theorem,
530 for cases of stationary and wall-sided bodies. Semi-analytical solutions of the mean
531 drift force on the compound column-plate structure are developed based on respectively
532 the derived and the classic far-field formulations. Those solutions both possess good
533 convergence and the results based on them agree well with each other.

534 2) The existence of the plate can notably disturb the wave scattering process related
535 to a column. At specific frequencies, obvious amplification of the free-surface
536 oscillation can be observed around the front and the rear edges of the column after
537 including the effects of the plate. Correspondingly, local pressure on the body can be
538 obviously increased, which is not beneficial to the structural safety.

539 3) In the horizontal direction, the linear wave force and mean drift force both increase
540 as the plate radius or height increases. In the vertical direction, the linear wave force
541 and mean drift force on a column with an attached plate follow a substantially different
542 behavior from that without the plate and can vanish at specific frequencies due to the
543 cancellation between the wave action on the bottom and the upper surfaces of the plate,
544 which suggests that the attached plate can be optimized to decrease the vertical force
545 through adjusting the design parameters.

546

547 **Acknowledgement**

548 The work is financial supported by the National Natural Science Foundation of China
549 (Grant Nos. 51479026 and 51679036).

550

551 **Reference**

- 552 1. [Antonutti R, Peyrard C, Johanning L, et al. An investigation of the effects of wind-induced](#)
553 [inclination on floating wind turbine dynamics: heave plate excursion. Ocean Engineering, 2014,](#)
554 [91\(15\): 208-217.](#)
- 555 2. [Bachynski E E, Kvittum M I, Luan C, et al. Wind-wave misalignment effects on floating wind](#)
556 [turbines: motions and tower load effects. Journal of Offshore Mechanics & Arctic Engineering,](#)
557 [2014, 136\(4\): 041902.](#)

- 558 3. Calisal S M, Sabuncu T. Hydrodynamic coefficients for vertical composite cylinders. *Ocean*
559 *Engineering*, 1984, 11(5): 525-542.
- 560 4. Chen X B. Middle-field formulation for the computation of wave-drift loads. *Journal of*
561 *Engineering Mathematics*, 2006, 59(1): 61-82.
- 562 5. Downie M J, Graham J M R, Hall C, et al. An experimental investigation of motion control
563 devices for truss spars. *Marine Structures*, 2000, 13(2): 75-90.
- 564 6. Farina L. Water wave radiation by a heaving submerged horizontal disk very near the free
565 surface. *Physics of Fluids*, 2010, 22(5): 057102.
- 566 7. Jiang S C, Gou Y and Teng B. Water Wave Radiation Problem by a Submerged Cylinder.
567 *Journal of Engineering Mechanics*, 2014, 140(5): 06014003.
- 568 8. Jiang S C, Gou Y, Teng B, et al. Analytical solution of a wave diffraction problem on a
569 submerged cylinder. *Journal of Engineering Mechanics*, 2014, 140(1): 225-232.
- 570 9. Koh H J and Cho I H. Heave motion response of a circular cylinder with the dual damping
571 plates. *Ocean Engineering*, 2016, 125: 95-102.
- 572 10. Lee C H. On the evaluation of quadratic forces on stationary bodies. *Journal of Engineering*
573 *Mathematics*, 2007, 58(1-4): 141-148.
- 574 11. Li B -B, Huang Z -H, Low Y M, et al. Experimental and numerical study of the effects of heave
575 plate on the motion of a new deep draft multi-spar platform. *Journal of Marine Science and*
576 *Technology*, 2013, 18(2): 229-246.
- 577 12. Martin P A and Farina L. Radiation of water waves by a heaving submerged horizontal disc.
578 *Journal of Fluid Mechanics*, 1997, 337: 365-379.
- 579 13. Maruo H. The drift of a body floating in waves. *Journal of Ship Research*, 1960, 4: 1-10.
- 580 14. Mei C C, Stiassnie M, Yue D K -P. Theory and applications of ocean surface waves. 2005,
581 World Scientific, Singapore.
- 582 15. Molin B. On the added mass and damping of periodic arrays of fully or partially porous disks.
583 *Journal of Fluids and Structures*, 2001, 15(2): 275-290.
- 584 16. Newman J N. The drift force and moment on ships in waves. *Journal of Ship Research*, 1967,
585 11: 51-60.
- 586 17. Ogilvie T F. Second order hydrodynamic effects on ocean platforms. In: Proceedings of
587 International Workshop on Ship and Platform Motions, University of California, Berkeley,
588 USA, Oct 26-28 1983, pp. 205-265.
- 589 18. Pinkster J A. Low frequency second order wave exciting forces on floating structures. PhD
590 Thesis, Delft University of Technology, the Netherlands, 1980.
- 591 19. Tao L -B, Thiagarajan K. Low KC flow regimes of oscillating sharp edges I. Vortex shedding
592 observation. *Applied Ocean Research*, 2003, 25(1): 21-35.
- 593 20. Tao L -B, Thiagarajan K. Low flow regimes of oscillating sharp edges. II. Hydrodynamic forces.
594 *Applied Ocean Research*, 2003, 25(2): 53-62.
- 595 21. Wang K, Zhang Z -Q. Study on hydrodynamic coefficients of double submerged inclined plates.
596 *China Ocean Engineering*, 2018, 32(1): 85-89.

- 597 22. Yeung R W. Added mass and damping of a vertical cylinder in finite-depth waters. Applied
598 Ocean Research, 1981, 3(3): 119-133.
- 599 23. Yu X -P. Functional performance of a submerged and essentially horizontal plate, for offshore
600 wave control: a review. Coastal Engineering Journal, 2002, 44(02): 127-147.
- 601 24. Yu X -P and Chwang A T. Analysis of wave scattering by submerged circular disk. Journal of
602 Engineering Mechanics, 1993, 119(9): 1804-1817.